

Visible to mid-IR Spectro-Microscopy with Top-Down Illumination and Nanoscale (≈ 10 nm) Resolution

Devon S. Jakob & Andrea Centrone*

Nanoscale Device Characterization Division, Physical Measurement Laboratory,
National Institute of Standards and Technology, 100 Bureau Drive, Gaithersburg, MD
20899, USA.

Email: andrea.centrone@nist.gov

Abstract

Photothermal induced resonance (PTIR), an atomic force microscopy (AFM) analogue of IR spectroscopy also known as AFM-IR, is capable of nanoscale lateral resolution and finds broad applications in biology and materials science. Here, the spectral range of a top-illumination PTIR setup operating in contact-mode is expanded for the first time to the visible and near-IR spectral ranges. The result is a tool that yields absorption spectra and maps of electronic and vibrational features with spatial resolution down to ≈ 10 nm. In addition to the improved resolution, the setup enables light-polarization dependent PTIR experiments in the visible and near-IR ranges for the first time. While previous PTIR implementations in the visible used total internal reflection illumination requiring challenging sample preparations on an optically transparent prism, the top-illumination used here greatly simplifies sample preparation and will foster a broad application of this method.

Introduction

Light-matter interactions provide access to compositional, structural, and physical properties of materials. For example, visible (≈ 400 nm to ≈ 780 nm) and near-IR (≈ 780 nm to ≈ 2.5 μm) spectroscopies aid the engineering of high-efficiency optoelectronic devices by identifying bandgaps, defects, and by characterizing optical excitations (i.e., excitons, plasmons).¹⁻³ In contrast, mid-IR (≈ 2.5 μm to ≈ 20 μm) spectroscopy provides information on compositions, chemical groups, molecular conformations, and polymorphisms, which are crucial for materials' optimization and for understanding biological processes.⁴⁻⁶ Device miniaturization and the advent of nanotechnology demands characterization of materials' properties with nanoscale resolution, an unattainable task for conventional far-field optical methods⁷⁻⁹ as their spatial resolution is limited by diffraction to approximately a half of the wavelength of light.¹⁰ The dependence of the spatial resolution on the wavelength also complicates correlations of optical and compositional properties across spectral ranges. Furthermore, for wavelengths comparable in size to sample features (chemical domains, roughness, etc.), spectral dispersions and shifts (related to both the real and imaginary parts of the refractive index) make chemical identification based on IR fingerprints (related exclusively the imaginary refractive index) difficult.

The photothermal induced resonance (PTIR) technique overcomes these limitations by employing the probe of an atomic force microscope (AFM) to transduce the photothermal expansion caused by the absorption of light pulses in the sample.¹¹⁻¹⁴ The high-sensitivity and bandwidth of custom AFM probes with built-in optical resonators can afford direct measurements of the nanoseconds-long sample thermal expansion,^{15,16} however, such impulses just kick conventional AFM probes into oscillation with amplitude

proportional to the absorbed energy in the sample.^{15,17,18} In first approximation, PTIR's direct sensitivity to the imaginary part of the sample's refractive index via the photothermal effect^{17,18} reliably yields chemical identification via IR-fingerprints.¹⁹ As the AFM tip mechanically transduces the light absorbed by the sample, PTIR's spatial resolution is wavelength-independent, reaching ≈ 5 nm in tapping-mode,²⁰ and ≈ 20 nm in contact-mode²¹; much lower than thermal diffusion-limited AFM methods.²² As discussed in recent reviews,¹¹⁻¹⁴ these characteristics together with the availability of different PTIR measurement modalities have propelled PTIR to impact a large number of applications in medicine,²³⁻²⁵ materials science,²⁶⁻²⁹ optics,³⁰⁻³² optoelectronics,³³ geology,^{34,35} among other fields. However, PTIR has been mainly restricted to the mid-IR spectral range due to the availability of commercial instrumentation in this range, and it is often referred to as AFM-IR.¹⁴ The recent extension of PTIR to the visible and near-IR spectral ranges by our group²¹ has enabled the characterizations of organic-inorganic perovskites^{29,33} and CdTe solar cells.³⁶ but has been constrained by the total internal reflection (TIR) sample illumination scheme employed.^{18,36} While TIR limits the AFM cantilever self-absorption background, it has the challenging requirement for preparing the sample on an optically transparent prism. Furthermore, the TIR evanescent-field illumination restricts the maximum sample thickness to ≈ 1 μm .¹⁸ In the mid-IR, PTIR is more commonly implemented with top illumination, but it requires using metal-coated AFM probes to limit the cantilever absorption background.³⁷ Although gold-coated cantilevers work well in the mid-IR, the extinction coefficient of gold is a non-monotonic function in the visible range which may distort the shape of PTIR absorption spectra in the visible range. Proof-of-principle PTIR measurements with top illumination using a gold-coated AFM probe and a

laser with fixed wavelength (671 nm) have been reported previously³⁸ but lacked spectroscopic capabilities to assess such effects.

Here, we integrate a visible/near-IR wavelength-tunable laser with a top-illumination, commercial PTIR setup and develop a series of motorized stages to precisely control the light position, intensity and polarization direction. We obtain an instrument capable of measuring absorption spectra and maps from 434 nm to 11.23 μm with a ≈ 10 nm wavelength-independent resolution, possibly the highest reported to date for contact-mode PTIR. As proof-of-principle, we measure electronic and vibrational features of an organic dye phase separated within a poly(methyl methacrylate) (PMMA) film. For this breakthrough we use uncoated dielectric (Si) AFM probes with low optical absorption, which yield high quality PTIR data of the sample absorption in the visible range which are not convoluted with the spectral response of the probe. Thanks to the simpler sample preparation requirements, we envision that this novel setup will enable PTIR characterizations on a broad range of optoelectronic and low-dimensional materials. Furthermore, while light polarization was uncontrolled in our previous PTIR experiments in the visible range, the newly introduced polarization control stages will facilitate studies on nanoscale optical anisotropies and permit the efficient excitation and detection of optical modes (e.g., exciton polaritons, phonon polaritons, plasmons).

Experimental Section

Laser Descriptions

The PTIR apparatus with top-down illumination developed in this work consists of an AFM, three wavelength-tunable lasers and motorized optics, housed in a nitrogen

purged enclosure (**Figure 1**). Protected silver mirrors were used throughout the setup. Here we integrate a commercially available laser consisting of a Q-switched diode-pumped Nd:YAG pump and a β -barium borate optical parametric oscillator (OPO), hereafter Laser-A. Laser-A emits 1 kHz narrow-bandwidth (<1 nm) light pulses (≈ 8 ns) with wavelength tunable from 405 nm to 2300 nm. Laser-A has two stages (signal and idler) that emit linearly polarized light either in the horizontal direction (405 nm to 709 nm, signal, s-polarization) or in the vertical direction (709 nm to 2300 nm, idler, p-polarization). The combination of optics used and the wavelength-dependent power output of laser-A provide for a usable spectral range from 434 nm to 2127 nm in PTIR experiments. Laser-B is a commercially available external-cavity mid-IR quantum cascade laser (QCL) consisting of four individual chips housed in a single enclosure. Laser-B emits narrowband (<1 cm^{-1}) light pulses (40 ns to 1000 ns) with a repetition rate tunable from 1 kHz up to 3 MHz and with a wavelength tunable from ≈ 5.4 μm to ≈ 11 μm (910 cm^{-1} – 1850 cm^{-1}). Laser-B emits linearly polarized light in the vertical direction (p-polarization). Laser-C is a custom, commercially sourced, intracavity OPO emitting 10 ns long narrowband (<10 cm^{-1}) pulses with a repetition rate tunable between 100 kHz and 250 kHz with a tunable wavelength between 2.5 μm and 3.7 μm (2700 cm^{-1} – 4000 cm^{-1}). Laser-C emits linearly polarized light in the vertical direction (p-polarization). All three lasers are shared with a TIR-illumination PTIR setup, which was described previously at an early stage of development.^{21,39} **Figure S1** of the supporting information shows the simplified schematic of the our entire PTIR apparatus which includes three additional lasers not employed in this report.

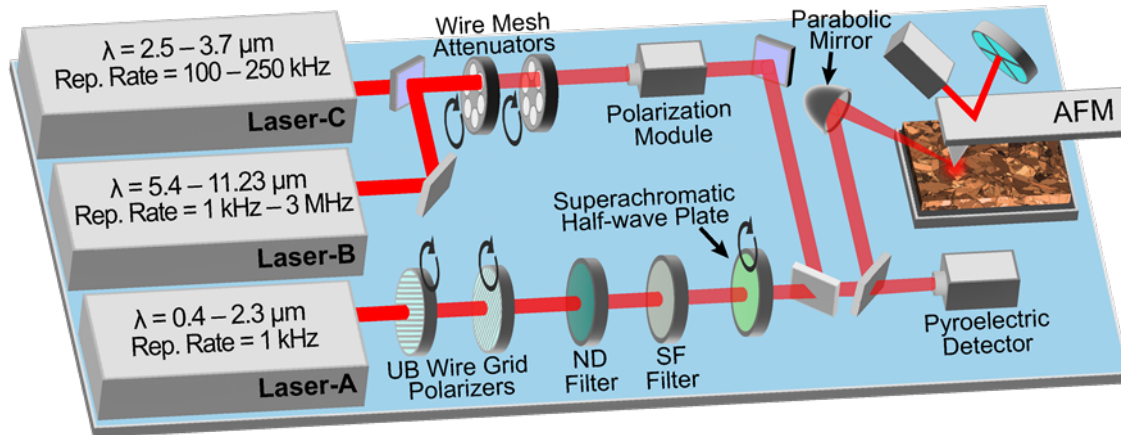


Figure 1. Simplified schematic for the PTIR apparatus with top-down illumination. The setup consists of three wavelength(λ)-tunable lasers (Lasers A, B, C), an atomic force microscope (AFM), and motorized optics used to align the laser light with respect to the AFM cantilever and to control the intensity and polarization of light. The setup is purged in dry nitrogen. A parabolic mirror focuses the laser light to a $\approx 30 \mu\text{m}$ wide spot centered around the AFM tip. All motorized stages are calibrated to maintain the beam position ($\pm 5 \mu\text{m}$) and light polarization ($\pm 1^\circ$) constant throughout the PTIR experiments. In the mid-IR, the light intensity is discretely attenuated using metallic wire meshes mounted on two filter wheels, while the polarization is controlled using reflecting optics. In the visible and near-IR ranges the light intensity is controlled using a custom-made spectral flattening (SF) filter, a neutral density (ND) filter, and two ultrabroadband (UB) wire grid polarizers. In these ranges, the polarization at the sample is controlled using the two UB wire grid polarizers in concert with a superachromatic half-wave plate.

Polarization and Intensity Control

The power of Laser-A (up to 500 mW) varies strongly with wavelength and must be substantially and precisely attenuated to avoid sample damage and to maximize the PTIR signal-to-noise ratio, respectively. This is accomplished using an absorptive neutral density filter (optical density – OD-0.9) and a custom-made spectral-flattening filter (OD between 0.046 and 1) in combination with two ultrabroadband (UB, 400 nm to 2200 nm) wire grid polarizers (≈ 10000 extinction ratio, fused silica substrate) mounted on fast ($115^\circ/\text{s}$) rotation stages. The first UB wire grid polarizer is rotated to continuously control the light intensity as a function of the rotation angle but also rotates the light polarization

direction. The second UB wire grid polarizer restores the light polarization direction as it is set with the maximum transmission parallel to the laser output polarization direction. To control the polarization direction at the sample precisely, we employ a superachromatic half-wave plate (wavelength-dependent retardation $<1^\circ$ between 600 nm and 2700 nm) that consists of 3 quartz and 3 magnesium fluoride plates cemented together, enabling accurate and continuous rotation of the light polarization direction. The positions of all those optical elements and motorized mirrors are calibrated and independently actuated to maintain the beam position ($\pm 5 \mu\text{m}$) and the light polarization direction ($\pm 1^\circ$) constant while sweeping the laser wavelength. Particularly, the light polarization direction at the sample position was measured as a function of wavelength and a calibration curve linking the half-wave plate rotation to the wavelength was constructed to minimize variations. Such calibration compensates for any wavelength-dependent polarization rotation induced by the reflective optics and to compensate for the non-negligible wavelength-dependent phase retardance of the half-wave plate between 400 nm and 600 nm. The light emitted by Lasers-B and -C is attenuated using 10 metal-wire mesh filters mounted on a pair of six-position motorized filter wheels, thus providing 36 discrete power levels. Their polarization at the sample is controlled using a commercially available motorized polarization module based on reflective optics.

PTIR Experimental Details

A series of flipper mirrors select and direct the light from one of the three lasers towards the sample, where it is focused to a $\approx 30 \mu\text{m}$ spot size by a 90° off-axis parabolic mirror and incident at 20° with respect to the sample surface. In this work, all PTIR measurements were carried out with p-polarization (unless otherwise noted) and in

contact-mode. In the mid-IR spectral range, commercially available gold-coated AFM probes (0.2 N/m nominal spring constant and ≈ 20 nm apex radius) were used. With Laser-B, we used a resonance enhanced detection scheme^{14,37} by matching the laser repetition rate to one of the AFM cantilever mechanical resonances (e.g., ≈ 186 kHz, **Figure S2**) and maintaining the enhancement with a phase-locked loop (PLL).²⁴ For Laser-C, we use an off-resonance detection scheme⁴⁰ by setting its repetition rate to 250 kHz. Unless otherwise noted, the scan rate for the mid-IR images was 0.1 Hz. Since the gold coating on the AFM probe has a non-monotonic refractive index and extinction coefficient in the visible range, for measurements with laser-A we used commercially available uncoated silicon probes (0.2 N/m nominal spring constant and ≈ 6 nm apex radius). All PTIR images in the visible and near-IR ranges were obtained in ringdown-mode¹⁸ (i.e., off-resonance, **Figure S3**) since the repetition rate of Laser-A (1 kHz) is much lower than the cantilever first contact resonance frequency (≈ 70 kHz).^{21,39} In this case, the PTIR signal is obtained either from the maximum peak-to-peak of the time-domain ringdown signal or from the maximum of one of the cantilever resonances in the frequency domain. A narrowband bandpass filter (30 kHz to 50 kHz) was centered on one of the cantilever resonances to increase the signal-to-noise ratio. PTIR maps in the visible and near-IR ranges were obtained by synchronously averaging the signal of 32 pulses using a scan rate of 0.03 Hz. PTIR spectra were obtained by measuring the PTIR signal while holding the AFM probe stationary and sweeping the laser wavelength at intervals of 2 cm^{-1} in the mid-IR, 50 cm^{-1} in the near-IR, and 100 cm^{-1} in the visible. The PTIR spectral intensities were normalized with respect to the laser output intensity (background) obtained with a broadband

(0.193 μm to 20 μm) pyroelectric detector in proximity of the sample. Five spectra were averaged in each location to improve the signal-to-noise ratio.

Results & Discussion

Absorption of visible and near-IR light by a material typically results in electronic excitations, which relax via electron-phonon coupling into vibrational excitations and heat on picosecond time scales.^{41,42} In the mid-IR, the sample vibrational modes are instead excited directly. Similarly, absorption of vibrational overtones and combination bands in the near-IR also would lead to direct vibrational excitation.⁴³ In PTIR experiments, either case leads to the rapid heating and thermal expansion of the sample which, in turn, excites the oscillation of the AFM cantilever.²¹ PTIR signal transduction details are discussed in full in the recent literature.^{14,44} As a proof-of-concept, we prepared a sample consisting of a commercially available polycyanine dye (IR Dye 9658, Adam Gates & Company) dispersed in PMMA, as described previously.²¹ The sample has a thickness up to 425 nm \pm 25 nm, as determined by AFM. Uncertainties through this report represent a single standard deviation. While PMMA is mostly transparent in the visible and near-IR, the dye absorbs strongly. **Figure 2** shows an irregular particle protruding from the film. Spectra obtained at selected locations (**Fig. 2d**) reveal the presence of the dye (peaks at 613 nm, 724 nm and 823 nm) within the protruding particle, based on its characteristic absorption spectrum.²¹ In contrast, the spectrum away from the protrusion (gray, location 3) does not show any absorption features, suggesting it is a location with just PMMA. PTIR absorption maps at 613 nm (**Fig 2b**) and at 823 nm (**Fig 2c**) identify the outline of a dye particle within the PMMA matrix. Interestingly, the absorption maps do not correlate perfectly with the sample topography (**Fig 2a**) suggesting that the protrusion doesn't

consist purely of a dye particle and that PMMA covers part of the particle surface. This is not surprising as PTIR is not a surface selective technique, but it probes the sample at depth typically exceeding 1 μm ,¹⁴ especially for ringdown excitation.^{14,18,30,45} As the PTIR probing depth is deeper than the film thickness, we interpret the small signal intensity variations as local variations of the relative dye and PMMA fractions under the tip (i.e., to the vertical compositional heterogeneity in the sample). From the PTIR image at 613 nm, we estimate the spatial resolution to be $17 \text{ nm} \pm 4 \text{ nm}$ as the distance, d , over which the PTIR signal changes from 80% to 20% of the maximum in five parallel line profiles (**Fig. 2e**). A separate map showing a dye particle entirely buried beneath the PMMA is shown in **Figure S4**.

The concerted use of the wire grid polarizers and of the half-wave plate introduced here enables control of light polarization at the sample in PTIR experiments in the visible a near-IR ranges for the first time. By adding light polarization controls, we envision that this setup will enable PTIR investigations of the orientation and anisotropy of crystalline materials and oriented structures.^{29,46,47} Light polarization also mildly enhances (1.5x to 10x) the PTIR signal intensity due to the field enhancement at the tip, which is a function of polarization and of the optical characteristics of the tip, sample, and substrate.^{48,49} The sample analyzed here has unknown stratification and consists of isotropic PMMA and the proprietary dye, which may or may not be isotropic. From the spectra with orthogonal polarizations (**Fig 2f**), and assuming a fully isotropic sample, we estimate the signal enhancement (2.2 ± 0.4) due to the lightning-rod effect, occurring when the light polarization component is aligned with the AFM tip (i.e., vertical). The estimate is based on the spectral comparison between 600 nm and 1500 nm and its single standard

deviation uncertainty is primarily determined by the uncertainty of the wavelength-dependent polarization direction ($\pm 1^\circ$). Orthogonal-polarization PTIR maps obtained at 724 nm are shown in **Figure S5**. Alternatively, the intensity changes and the small spectral shifts for the spectra with orthogonal polarization (**Fig 2f**) could be attributed to the anisotropy of the dye phase.⁵⁰

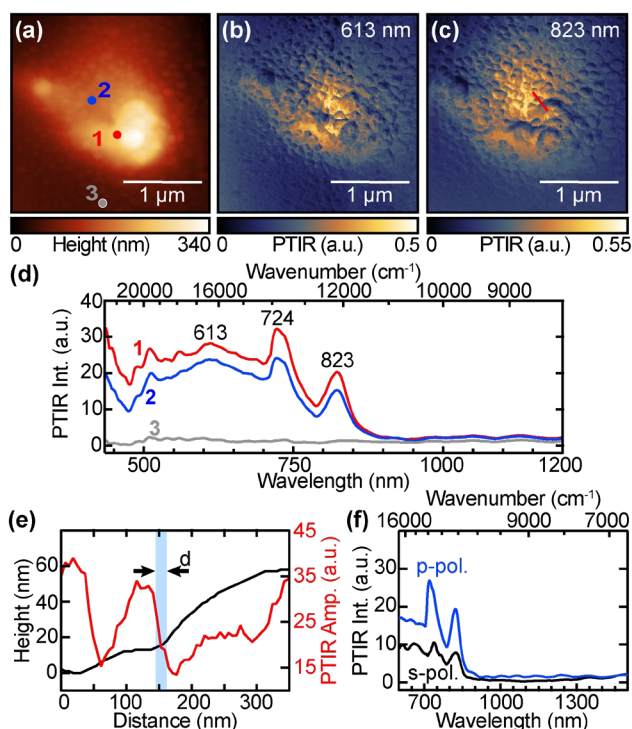


Figure 2. (a) AFM topography and corresponding PTIR absorption maps at (b) 613 nm and (c) 823 nm. Scale bars are 1 μm and the pixel sizes are 9.8 nm and 5.6 nm in the horizontal and vertical (scan) directions, respectively. (d) PTIR spectra obtained at the color-coded locations in panel-(a). (e) Topography (black) and PTIR line profiles corresponding to the location marked by the red line in (b). A PTIR spatial resolution, $d = 17 \text{ nm} \pm 4 \text{ nm}$ (blue background) was estimated from five adjacent line profiles. (f) PTIR spectra obtained at location-2 at orthogonal polarization directions.

PTIR measurements in the mid-IR (i.e., with Lasers-B and -C) on the same location are reported in **Figure 3**. Since the chemical structure of the proprietary polycyanine dye is unknown, we measured PTIR spectra (**Fig. 3a**) to better understand the composition

and distribution of the two phases. For comparison, the Fourier-transform infrared (FTIR) spectrum of the dye obtained with a diamond TIR accessory is shown in **Figure S6**. In the C-H stretching region (2700 cm^{-1} to 3100 cm^{-1}), the spectra are dominated by the characteristic PMMA absorption peaks, suggesting that some PMMA is present in each location, i.e., the thickness of the dye particle is smaller than the film thickness. The PTIR map at 2966 cm^{-1} (**Fig. 3c**) confirms this explanation. We interpret the map intensity variations as variations in the sample thickness convoluted with variations of the average composition at each location due to the vertical heterogeneity of the sample. While PMMA absorption features (see gray spectrum, location 3), are also the strongest in the IR fingerprint region, the red spectrum (location 1) shows additional discernable features, namely peaks at 1094 cm^{-1} , 1119 cm^{-1} , 1321 cm^{-1} , 1335 cm^{-1} , 1409 cm^{-1} , 1458 cm^{-1} , 1573 cm^{-1} , 1589 cm^{-1} and 1601 cm^{-1} which are assigned to the polycyanine dye. The most prominent peaks at $\approx 1315\text{ cm}^{-1}$ and the broad feature between 1560 cm^{-1} and 1620 cm^{-1} are also clearly visible, although with much lower intensity for the blue spectrum (location 2). The maps of these characteristic absorptions (1590 cm^{-1} in **Fig. 3d** and 1315 cm^{-1} in **Fig. 3e**) appear more localized than in Fig. 2. In contrast to the visible PTIR map at 613 nm (Fig. 2b) which shows low absorption for the small globular features, the images in Fig. 3 show strong absorption in correspondence of these features. We speculate that perhaps some of these characteristic peaks are related to a dye degradation product close to the sample surface. **Fig. 3f-g** highlights an isolated single protruding particle that we used to estimate the PTIR spatial resolution. By comparing topographic (Fig. 3f) and PTIR (Fig. 3g) line scans, the PTIR resolution is evidently better than the topography resolution. We estimate the PTIR resolution as $8.6\text{ nm} \pm 1.1\text{ nm}$ as the distance, d , over

which the PTIR signal changes from 80% to 20% of the maximum in five adjacent signal cross sections (**Fig. 3h**). Although the resolutions of Fig. 2 and Fig. 3 are comparable, the finer pixel resolution and higher signal-to noise ratio of Fig. 3 allow a more accurate estimate.

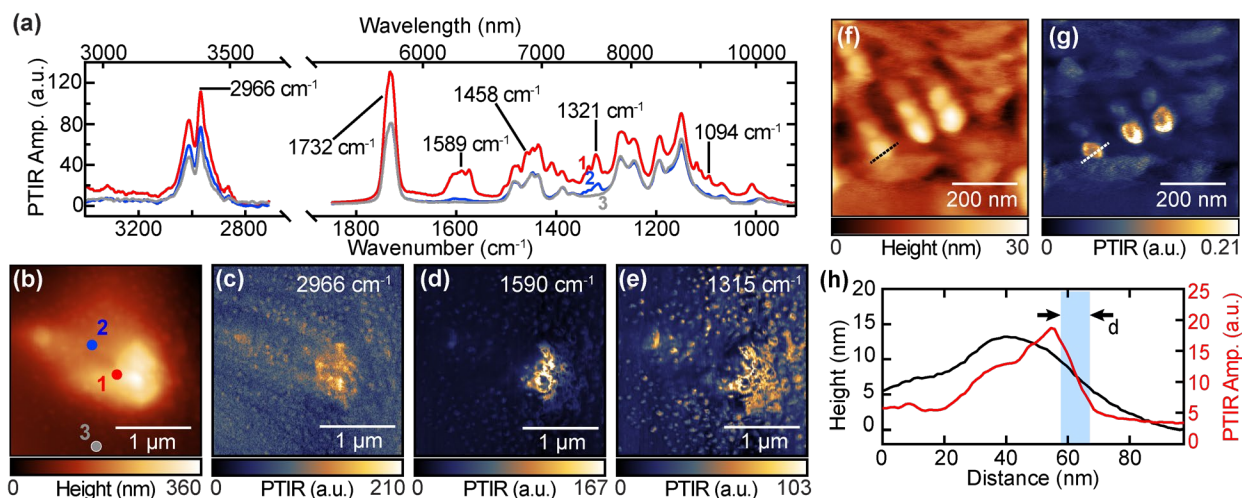


Figure 3. (a) PTIR spectra obtained at the color-coded locations in panel-b. (b) topography of the dye-loaded PMMA sample. Corresponding PTIR absorption maps at (c) 2966 cm^{-1} , PMMA aliphatic C-H stretching, (d) 1590 cm^{-1} , and (e) 1315 cm^{-1} , attributed to the polycyanine dye or derived product. Scale bars are 1 μm and the pixel sizes are 9.8 nm and 7.8 nm in the horizontal and vertical (scan) directions, respectively. (f) Topography and (g) corresponding PTIR absorption map at 1315 cm^{-1} of small protruding features in the sample. The scale bars are 200 nm and the pixel sizes are 1.2 nm and 1.6 nm in the horizontal (scan) and vertical directions, respectively. (h) Topography (black) and PTIR line profiles corresponding to the location marked by the black line in (f). A PTIR spatial resolution, $d = 8.6 \text{ nm} \pm 1.1 \text{ nm}$ (blue background) was estimated from five adjacent line profiles. The scan rate was 0.1 Hz for panels (b-e) and 0.06 Hz for panels (f-g).

Conclusions

In this work, a wavelength tunable laser was integrated with a top-illumination PTIR setup to extend its spectral range to visible and near-IR ranges for the first time. The resulting table-top PTIR setup can measure vibrational and electronic absorption spectra

and maps across a wide spectral range (434 nm to 11.23 μm) with ≈ 10 nm spatial resolution, i.e., besting our previous results²¹ in contact-mode. Furthermore, we developed motorized optical stages that, via calibration, maintain the laser alignment with respect to the AFM tip, and the light polarization direction at the sample constant. The new tool enables measurements of composition (mid-IR) and electronic absorption properties (visible, near-IR) at the nanoscale as a function of light polarization. Since the top illumination scheme adopted bypasses the requirement for sample preparations on an optically transparent prism, we envision a broad impact for this setup in applications ranging from materials science to optoelectronics, among others.

Supporting Information

Schematic of the whole PTIR apparatus, representative signal for resonance-enhanced PTIR, representative signal for ringdown PTIR, PTIR map of a subsurface dye particle, PTIR maps with orthogonal light polarization directions, and comparison of PTIR and FTIR spectra of the dye.

Additional Note

The materials used in this paper require the identification of a commercial product and its supplier. The inclusion of such information should in no way be construed as indicating that such product or supplier is endorsed by NIST or is recommended by NIST or that is necessarily the best material for the purpose described.

References

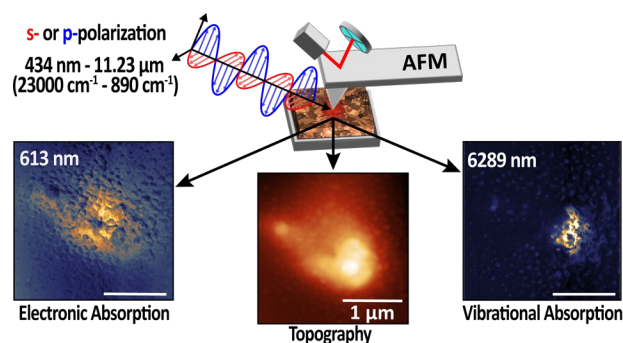
1. Zhang, L.; Ran, J.; Qiao, S.-Z.; Jaroniec, M., Characterization of Semiconductor Photocatalysts. *Chem. Soc. Rev.* **2019**, *48* (20), 5184-5206.

2. Chouhan, L.; Ghimire, S.; Subrahmanyam, C.; Miyasaka, T.; Biju, V., Synthesis, Optoelectronic Properties and Applications of Halide Perovskites. *Chem. Soc. Rev.* **2020**, *49* (10), 2869-2885.
3. Kalyanasundaram, K.; Grätzel, M., Applications of Functionalized Transition Metal Complexes in Photonic and Optoelectronic Devices. *Coord. Chem. Rev.* **1998**, *177* (1), 347-414.
4. Barth, A., Infrared Spectroscopy of Proteins. *Biochim. Biophys. Acta Bioenerg.* **2007**, *1767* (9), 1073-1101.
5. Wrobel, T. P.; Bhargava, R., Infrared Spectroscopic Imaging Advances as an Analytical Technology for Biomedical Sciences. *Anal. Chem.* **2018**, *90* (3), 1444-1463.
6. Kazarian, S. G.; Chan, K. A., Micro-and Macro-Attenuated Total Reflection Fourier Transform Infrared Spectroscopic Imaging: Plenary Lecture at the 5th International Conference on Advanced Vibrational Spectroscopy, 2009, Melbourne, Australia. *Appl. Spectrosc.* **2010**, *64* (5), 135A-152A.
7. Usman, M.; Mendiratta, S.; Lu, K. L., Semiconductor Metal–Organic Frameworks: Future Low-Bandgap Materials. *Adv. Mater.* **2017**, *29* (6), 1605071.
8. Koenderink, A. F.; Alù, A.; Polman, A., Nanophotonics: Shrinking Light-Based Technology. *Science* **2015**, *348* (6234), 516-521.
9. Tennyson, E. M.; Howard, J. M.; Leite, M. S., Mesoscale Functional Imaging of Materials for Photovoltaics. *ACS Energy Lett.* **2017**, *2* (8), 1825-1834.
10. Abbe, E., Beiträge zur Theorie des Mikroskops und der Mikroskopischen Wahrnehmung. *Arch. Mikr. Anat.* **1873**, *9* (1), 413-468.
11. Centrone, A., Infrared Imaging and Spectroscopy Beyond the Diffraction Limit. *Annu. Rev. Anal. Chem.* **2015**, *8*, 101-126.
12. Kurouski, D.; Dazzi, A.; Zenobi, R.; Centrone, A., Infrared and Raman Chemical Imaging and Spectroscopy at the Nanoscale. *Chem. Soc. Rev.* **2020**, *49* (11), 3315-3347.
13. Mathurin, J.; Deniset-Besseau, A.; Bazin, D.; Dartois, E.; Wagner, M.; Dazzi, A., Photothermal AFM-IR Spectroscopy and Imaging: Status, Challenges, and Trends. *J. Appl. Phys.* **2022**, *131* (1), 010901.
14. Schwartz, J. J.; Jakob, D. S.; Centrone, A., A Guide to Nanoscale IR Spectroscopy: Resonance Enhanced Transduction in Contact and Tapping Mode AFM-IR. *Chem. Soc. Rev.* **2022**, *51* (13), 5248-5267.
15. Chae, J.; An, S.; Ramer, G.; Stavila, V.; Holland, G.; Yoon, Y.; Talin, A. A.; Allendorf, M.; Aksyuk, V. A.; Centrone, A., Nanophotonic Atomic Force Microscope Transducers Enable Chemical Composition and Thermal Conductivity Measurements at the Nanoscale. *Nano Lett.* **2017**, *17* (9), 5587-5594.
16. Wang, M.; Ramer, G.; Perez-Morelo, D. J.; Pavlidis, G.; Schwartz, J. J.; Yu, L.; Ilic, R.; Aksyuk, V. A.; Centrone, A., High Throughput Nanoimaging of Thermal Conductivity and Interfacial Thermal Conductance. *Nano Lett.* **2022**.
17. Dazzi, A.; Glotin, F.; Carminati, R., Theory of Infrared Nanospectroscopy by Photothermal Induced Resonance. *J. Appl. Phys.* **2010**, *107* (12), 124519.
18. Lahiri, B.; Holland, G.; Centrone, A., Chemical Imaging Beyond the Diffraction Limit: Experimental Validation of the PTIR Technique. *Small* **2013**, *9* (3), 439-445.
19. Ramer, G.; Aksyuk, V. A.; Centrone, A., Quantitative Chemical Analysis at the Nanoscale Using the Photothermal Induced Resonance Technique. *Anal. Chem.* **2017**, *89* (24), 13524-13531.
20. Ma, X.; Pavlidis, G.; Dillon, E.; Beltran, V.; Schwartz, J. J.; Thoury, M.; Borondics, F.; Sandt, C.; Kjoller, K.; Berrie, B., Micro to Nano: Multiscale IR Analyses Reveal Zinc Soap Heterogeneity in a 19th-Century Painting by Corot. *Anal. Chem.* **2022**, *94* (7), 3103-3110.
21. Katzenmeyer, A. M.; Holland, G.; Kjoller, K.; Centrone, A., Absorption Spectroscopy and Imaging from the Visible Through Mid-Infrared with 20 nm Resolution. *Anal. Chem.* **2015**, *87* (6), 3154-3159.
22. Katzenmeyer, A. M.; Holland, G.; Chae, J.; Band, A.; Kjoller, K.; Centrone, A., Mid-Infrared Spectroscopy Beyond the Diffraction Limit via Direct Measurement of the Photothermal Effect. *Nanoscale* **2015**, *7* (42), 17637-17641.

23. Ruggeri, F. S.; Habchi, J.; Chia, S.; Horne, R. I.; Vendruscolo, M.; Knowles, T. P., Infrared Nanospectroscopy Reveals the Molecular Interaction Fingerprint of an Aggregation Inhibitor with Single A β 42 Oligomers. *Nat. Commun.* **2021**, *12* (1), 1-9.
24. Wieland, K.; Ramer, G.; Weiss, V. U.; Allmaier, G.; Lendl, B.; Centrone, A., Nanoscale Chemical Imaging of Individual Chemotherapeutic Cytarabine-Loaded Liposomal Nanocarriers. *Nano Res.* **2019**, *12* (1), 197-203.
25. Dou, T.; Li, Z.; Zhang, J.; Evilevitch, A.; Kurouski, D., Nanoscale Structural Characterization of Individual Viral Particles Using Atomic Force Microscopy Infrared Spectroscopy (AFM-IR) and Tip-Enhanced Raman Spectroscopy (TERS). *Anal. Chem.* **2020**, *92* (16), 11297-11304.
26. Katzenmeyer, A. M.; Canivet, J.; Holland, G.; Farrusseng, D.; Centrone, A., Assessing Chemical Heterogeneity at the Nanoscale in Mixed-Ligand Metal–Organic Frameworks with the PTIR Technique. *Angew. Chem. Int. Ed.* **2014**, *53* (11), 2852-2856.
27. Delen, G.; Ristanović, Z.; Mandemaker, L. D.; Weckhuysen, B. M., Mechanistic Insights into Growth of Surface-Mounted Metal-Organic Framework Films Resolved by Infrared (Nano-) Spectroscopy. *Eur. J. Chem.* **2018**, *24* (1), 187-195.
28. Morsch, S.; Lyon, S.; Gibbon, S., The Degradation Mechanism of an Epoxy-Phenolic Can Coating. *Prog. Org. Coat.* **2017**, *102*, 37-43.
29. Strelcov, E.; Dong, Q.; Li, T.; Chae, J.; Shao, Y.; Deng, Y.; Gruverman, A.; Huang, J.; Centrone, A., CH₃NH₃PbI₃ Perovskites: Ferroelasticity Revealed. *Sci. Adv.* **2017**, *3* (4), e1602165.
30. Schwartz, J. J.; Le, S. T.; Krylyuk, S.; Richter, C. A.; Davydov, A. V.; Centrone, A., Substrate-Mediated Hyperbolic Phonon Polaritons in MoO₃. *Nanophotonics* **2021**, *10* (5), 1517-1527.
31. Gallacher, K.; Millar, R. W.; Paul, D. J.; Frigerio, J.; Ballabio, A.; Isella, G.; Rusconi, F.; Biagioni, P.; Giliberti, V.; Sorgi, A., Characterization of Integrated Waveguides by Atomic-Force-Microscopy-Assisted Mid-Infrared Imaging and Spectroscopy. *Opt. Express* **2020**, *28* (15), 22186-22199.
32. Khanikaev, A. B.; Arju, N.; Fan, Z.; Purtseladze, D.; Lu, F.; Lee, J.; Sarriugarte, P.; Schnell, M.; Hillenbrand, R.; Belkin, M., Experimental Demonstration of the Microscopic Origin of Circular Dichroism in Two-Dimensional Metamaterials. *Nat. Commun.* **2016**, *7* (1), 1-8.
33. Chae, J.; Dong, Q.; Huang, J.; Centrone, A., Chloride Incorporation Process in CH₃NH₃PbI_{3-x}Cl_x Perovskites via Nanoscale Bandgap Maps. *Nano Lett.* **2015**, *15* (12), 8114-8121.
34. Kebukawa, Y.; Kobayashi, H.; Urayama, N.; Baden, N.; Kondo, M.; Zolensky, M. E.; Kobayashi, K., Nanoscale Infrared Imaging Analysis of Carbonaceous Chondrites to Understand Organic-Mineral Interactions During Aqueous Alteration. *Proc. Natl. Acad. Sci. U.S.A.* **2019**, *116* (3), 753-758.
35. Yang, J.; Hatcherian, J.; Hackley, P. C.; Pomerantz, A. E., Nanoscale Geochemical and Geomechanical Characterization of Organic Matter in Shale. *Nat. Commun.* **2017**, *8* (1), 1-9.
36. Yoon, Y.; Chae, J.; Katzenmeyer, A. M.; Yoon, H. P.; Schumacher, J.; An, S.; Centrone, A.; Zhitenev, N., Nanoscale Imaging and Spectroscopy of Band Gap and Defects in Polycrystalline Photovoltaic Devices. *Nanoscale* **2017**, *9* (23), 7771-7780.
37. Lu, F.; Jin, M.; Belkin, M., Tip-Enhanced Infrared Nanospectroscopy via Molecular Expansion Force Detection. *Nat. Photonics* **2014**, *8* (4), 307-312.
38. Zhou, J.; Smirnov, A.; Dietler, G.; Sekatskii, S. K., Gap-Plasmon-Enhanced High-Spatial-Resolution Imaging by Photothermal-Induced Resonance in the Visible Range. *Nano Lett.* **2019**, *19* (11), 8278-8286.
39. Katzenmeyer, A. M.; Aksyuk, V.; Centrone, A., Nanoscale Infrared Spectroscopy: Improving the Spectral Range of the Photothermal Induced Resonance Technique. *Anal. Chem.* **2013**, *85* (4), 1972-1979.
40. Kenkel, S.; Mittal, A.; Mittal, S.; Bhargava, R., Probe–Sample Interaction-Independent Atomic Force Microscopy–Infrared Spectroscopy: Toward Robust Nanoscale Compositional Mapping. *Anal. Chem.* **2018**, *90* (15), 8845-8855.

41. Chen, S.; Lee, I. S.; Tolbert, W. A.; Wen, X.; Dlott, D. D., Applications of Ultrafast Temperature Jump Spectroscopy to Condensed Phase Molecular Dynamics. *J. Phys. Chem.* **1992**, *96* (18), 7178-7186.
42. Chang, T. C.; Dlott, D. D., Vibrational Cooling in Large Molecular Systems: Pentacene in Naphthalene. *Chem. Phys.* **1989**, *90* (7), 3590-3602.
43. Workman Jr, J. J., Interpretive Spectroscopy for Near Infrared. *Appl. Spectrosc. Rev.* **1996**, *31* (3), 251-320.
44. Schwartz, J. J.; Pavlidis, G.; Centrone, A., Understanding Cantilever Transduction Efficiency and Spatial Resolution in Nanoscale Infrared Microscopy. *Anal. Chem.* **2022**, *94* (38), 13126-13135.
45. Schwartz, J. J.; Chuang, H.-J.; Rosenberger, M. R.; Sivaram, S. V.; McCreary, K. M.; Jonker, B. T.; Centrone, A., Chemical Identification of Interlayer Contaminants Within Van der Waals Heterostructures. *ACS Appl. Mater. Interfaces* **2019**, *11* (28), 25578-25585.
46. Gong, L.; Chase, D. B.; Noda, I.; Marcott, C. A.; Liu, J.; Martin, D. C.; Ni, C.; Rabolt, J. F., Polymorphic Distribution in Individual Electrospun Poly [(R)-3-Hydroxybutyrate-Co-(R)-3-Hydroxyhexanoate](PHBHx) Nanofibers. *Macromolecules* **2017**, *50* (14), 5510-5517.
47. Wang, Z.; Sun, B.; Lu, X.; Wang, C.; Su, Z., Molecular Orientation in Individual Electrospun Nanofibers Studied by Polarized AFM-IR. *Macromolecules* **2019**, *52* (24), 9639-9645.
48. Wang, C.-T.; Jiang, B.; Zhou, Y.-W.; Jiang, T.-W.; Liu, J.-H.; Zhu, G.-D.; Cai, W.-B., Exploiting the Surface-Enhanced IR Absorption Effect in the Photothermally Induced Resonance AFM-IR Technique Toward Nanoscale Chemical Analysis. *Anal. Chem.* **2019**, *91* (16), 10541-10548.
49. Waeytens, J.; Mathurin, J.; Deniset-Besseau, A.; Arluison, V.; Bousset, L.; Rezaei, H.; Raussens, V.; Dazzi, A., Probing Amyloid Fibril Secondary Structures by Infrared Nanospectroscopy: Experimental and Theoretical Considerations. *Analyst* **2021**, *146* (1), 132-145.
50. Mayerhöfer, T. G., *Wave Optics in Infrared Spectroscopy*. 2021; DOI: 10.13140/RG.2.2.14293.55520.

For Table of Contents Only



Supporting Information

Visible to mid-IR Spectro-Microscopy with Top-Down Illumination and Nanoscale (≈ 10 nm) Resolution

Devon S. Jakob & Andrea Centrone*

Nanoscale Device Characterization Division, Physical Measurement Laboratory,
National Institute of Standards and Technology, 100 Bureau Drive, Gaithersburg, MD
20899, USA.

Email: andrea.centrone@nist.gov

Table of Contents

Figure S1: Schematic of the whole PTIR apparatus.....	2
Figure S2: Representative signal for resonance-enhanced PTIR	3
Figure S3: Representative signal for ringdown PTIR.....	4
Figure S4: PTIR map of a subsurface dye particle.....	4
Figure S5: PTIR maps with orthogonal light polarization directions	5
Figure S6: Comparison of PTIR and FTIR spectra of the dye.....	5

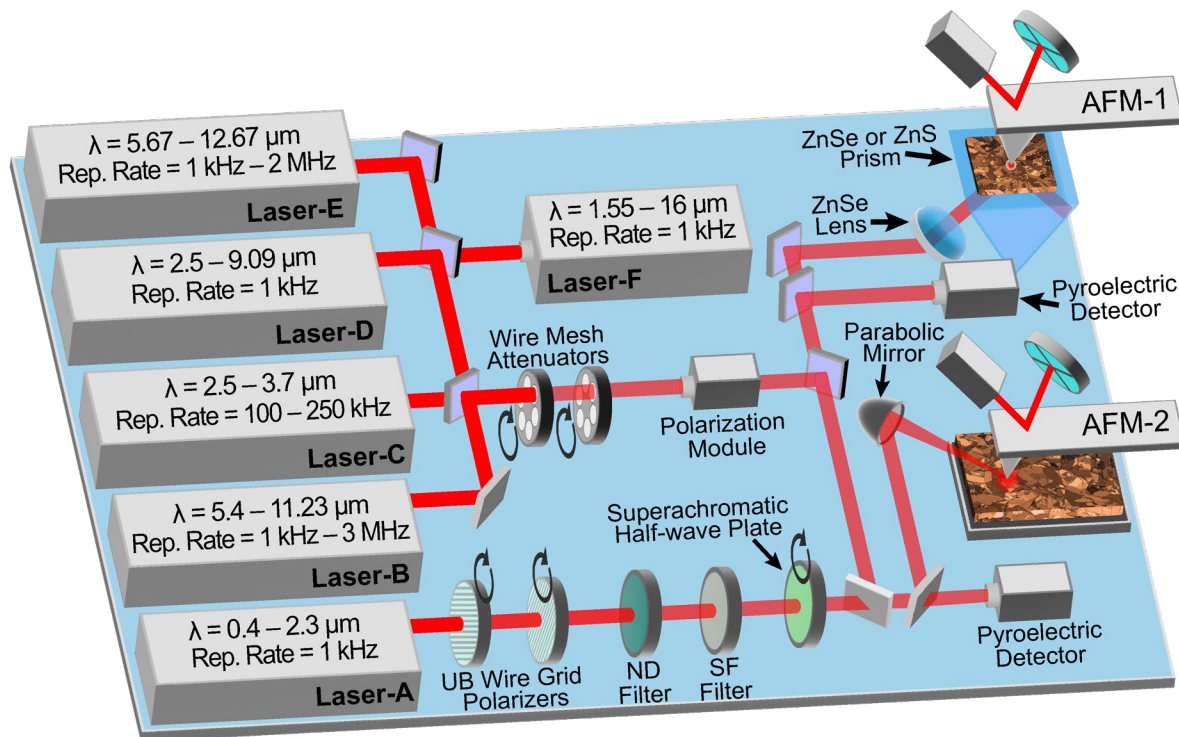


Figure S1. Simplified schematic of the full, dry nitrogen purged PTIR apparatus in our lab. The setup consists of six wavelength(λ)-tunable lasers (Lasers A, B, C, D, E, F), two atomic force microscopes (AFM-1, AFM-2), and motorized optics used to align the laser light and to control the intensity and polarization of light. Motorized flipper mirrors select and direct the light from one of the six lasers towards either the AFM-1, where the sample is illuminated from below with total internal reflection (TIR), or towards the AFM-2, where the sample is illuminated from the top. Lasers-A, -B, and -C are described in the main text. Laser-D consists of a Q-switched diode-pumped Nd:YAG laser, pumping a periodically poled lithium niobate (PPLN) OPO which pumps a ZnGeP₂ OPO. Laser-D emits narrowband (between 5 cm⁻¹ and 16 cm⁻¹) 10 ns pulses continuously tunable from 2.5 μm to 9.09 μm at a fixed repetition rate of 1 kHz. Laser-E is an external-cavity mid-IR QCL consisting of four chips housed in a single enclosure. Laser-E emits narrowband (1 cm⁻¹) light pulses (40 ns to 500 ns) with tunable output between 5.67 μm and 12.67 μm at a repetition rate tunable from 1 kHz to 2 MHz. Laser-F consists of a mode-locked Nd:YVO₄ pump laser which drives a synchronously pumped PPLN OPO, a KTiOAsO₄ optical parametric amplifier, and a GaSe difference frequency generation stage. Laser-F emits 100 ps narrowband (0.5 cm⁻¹) pulses at a fixed repetition rate of 1 kHz. A ZnSe lens is used to focus the light under the AFM tip in AFM-1, which can be used in combination with lasers A, B, C, D, E and F and requires preparing the sample on a ZnSe or ZnS optical prism. A parabolic mirror focuses the laser light centered around the AFM tip in AFM-2 which can be used in combination of laser A, B, C as described in detail in the main text. All motorized stages are calibrated to maintain the beam position and light polarization constant throughout the PTIR experiments as described in the main text.

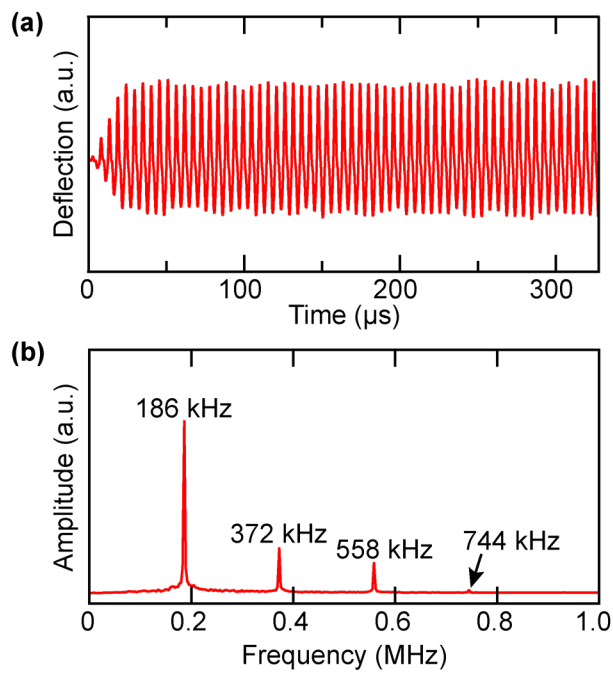


Figure S2. (a) Time-domain resonance-enhanced PTIR signal obtained by matching the laser pulse repetition rate to one of the mechanical resonances of the AFM cantilever (186 kHz). (b) Frequency-domain resonance-enhanced PTIR signal amplitude. A narrowband bandpass filter (38 kHz) was centered at 186 kHz.

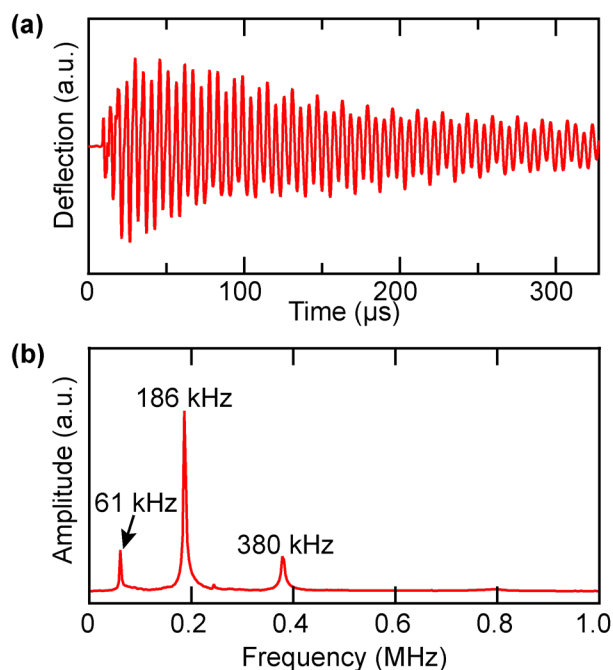


Figure S3. (a) Time-domain PTIR signal (ringdown) obtained with a laser pulse repetition rate (1 kHz) much lower than the cantilever mechanical resonances. (b) Corresponding frequency-domain PTIR signal amplitude. A narrowband bandpass filter (38 kHz) was centered at 186 kHz.

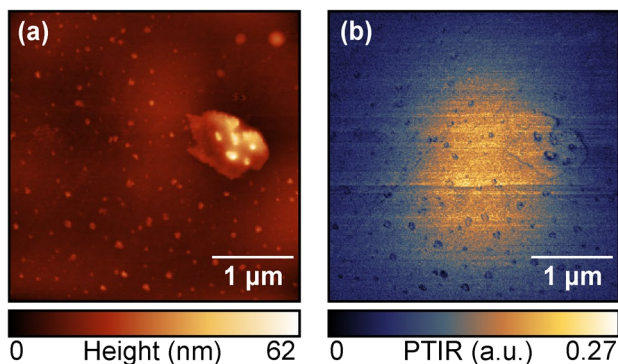


Figure S4. (a) Topography and (b) PTIR image obtained at 613 nm reveals high absorption signal originating from below the surface of the phase-separated polycyanine dye within the PMMA matrix, which is attributed to a dye particle buried entirely beneath a layer of PMMA. The pixel sizes are 13.9 nm and 9.2 nm in the horizontal and vertical (scan) directions, respectively. The scale bar is 1 μm. The scan rate was 0.04 Hz.

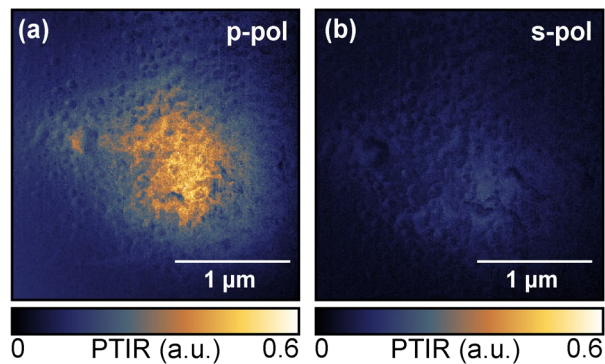


Figure S5. PTIR absorption images at 723 nm for (a) p-polarization and (b) s-polarization on the dye-loaded PMMA sample. The pixel sizes are 9.8 nm and 5.9 nm in the horizontal and vertical (scan) directions, respectively. The scale bar is 1 μm . The scan rate was 0.03 Hz.

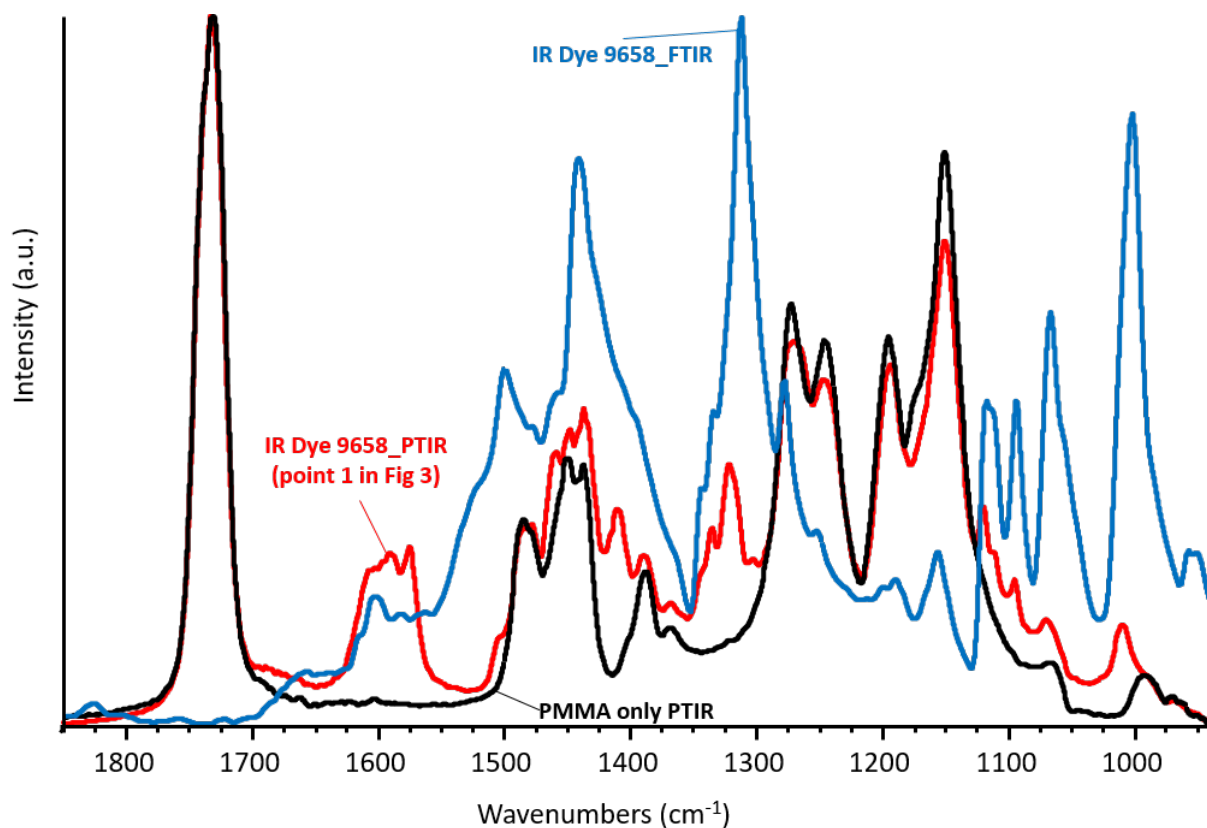


Figure S6. PTIR spectra of the dye-loaded PMMA sample at two locations (red and black) and FTIR spectrum of the pure dye powder (blue). The PTIR spectra are from Fig. 3 of the main text. The FTIR spectrum is averaged from 128 scans with a spectral resolution of 4 cm^{-1} and is obtained using a commercially available FTIR spectrometer with an attenuated total reflection accessory (diamond crystal) and a KBr beam splitter. All spectra are normalized.

